Research Square

Preprints are preliminary reports that have not undergone peer review.
They should not be considered conclusive, used to inform clinical practice,
or referenced by the media as validated information.

CFD-informed machine learning for surface-temperature mapping of side-cooled 4680 lithium-ion cells under thermal uncertainty

Aydin Ulus
Youngstown State University
Ihsan Uluocak
Cukurova University
Wajih Nazim Kamal
Youngstown State University
Kyosung Choo
Youngstown State University
Young Jik Youn
yjyoun@hanbat.ac.kr

Hanbat National University

Article

Keywords: 4680 lithium-ion battery, thermal management, CFD, machine learning, surface temperature, heat exchange

Posted Date: November 4th, 2026

DOI: https://doi.org/10.21203/rs.3.rs-11158435/v1

License: This work is licensed under a Creative Commons Attribution 4.0 International License.
Read Full License

Additional Declarations: No competing interests reported.

Abstract

Large-format 4680 lithium-ion cells present a thermal-monitoring challenge because surface measurements do not fully describe the temperature field and key heat-transfer properties remain uncertain. This study combines a validated three-dimensional steady thermal model with machine learning to reconstruct the external can-surface temperature field of a side-cooled 4680 cell. Seventy-five CFD cases were generated by varying radial jelly-roll conductivity from 0.90 to 2.00 W m^{-1} K^{-1} and equivalent interface thickness from 0.40 to 0.60 mm at a fixed 6.0 W heat input and 25°C cooling boundary. Temperatures from 25 surface locations produced 1,875 spatial samples. The CFD model reproduced three published validation temperatures within 0.196°C, and the two finest meshes differed by less than 0.01%. CNN-LSTM and SVM yielded similar held-out point-level performance, with R^2 values of 0.981 and 0.980 and RMSE values of 0.238 and 0.245°C, respectively; MLP was less accurate. Feature perturbation identified axial position as the dominant predictor, followed by x-position and radial conductivity. The resulting surrogate reproduces the simulated can-surface temperature field within the investigated steady-state parameter range and provides a computationally inexpensive basis for thermal-sensitivity analysis.

1. Introduction

Temperature has a direct influence on lithium-ion battery performance, degradation, and safety. The temperature reached during operation is set by the balance between electrochemical heat generation and heat removal, while the internal temperature field depends on the geometry and thermal properties of the cell [1, 2]. The resulting spatial gradients are also important. Experiments have shown that non-uniform temperature can change cell impedance and electrochemical response, and that the magnitude and direction of thermal gradients depend on cell design and operating conditions [3, 4]. Surface measurements therefore provide only a partial description of the thermal state, particularly when appreciable temperature gradients develop inside the cell.

Cell size adds another constraint to thermal management. The 4680 format combines a 46 mm diameter with an 80 mm height, increasing the amount of active material per cell but also increasing the radial distance over which internally generated heat must be conducted. Early modeling of the format showed that conventional tab-based current collection can produce substantial electrical and thermal non-uniformity, whereas continuous or tabless current collection reduces current-collector losses and heat generation [5]. Teardown and characterization of production Tesla 4680 cells subsequently confirmed the distinctive large-format architecture and reported strong surface heating during high-rate charging without active cooling [6]. Three-dimensional electro-thermal analysis has further shown that large cylindrical cells cannot be treated simply as scaled versions of 18650 or 21700 cells because cell size, internal current-collection paths, anisotropic heat conduction, and the selected cooling surface interact in determining the thermal response [7].

Recent work has consequently focused on thermal management strategies tailored to the 4680 format. Allgäuer et al. combined thermal measurements with a validated three-dimensional model and found that, for the investigated 4680 cell, side cooling produced lower surface temperatures than bottom cooling, while cooling a larger portion of the mantle surface improved heat rejection further [8]. Their later fast-charging study showed that the thermal boundary condition also affects internal gradients and degradation behavior [9]. A recent CFD comparison of sided and terminal cold-plate layouts likewise reported lower peak temperatures and smaller temperature spreads for sided configurations under the conditions examined [10]. Other studies have investigated two-phase immersion cooling and extreme-fast-charging operation, demonstrating both the benefit of aggressive cooling and the continuing sensitivity of 4680 cells to temperature non-uniformity [11, 12]. Together, these studies indicate that the temperature field depends on both the imposed heat generation and the resistance of the heat-transfer path between the jelly roll and the cooling boundary.

Considerable uncertainty remains in the thermal properties that define these heat-transfer paths. Cylindrical jelly rolls are strongly anisotropic because radial heat flow crosses repeated electrode, separator, electrolyte, and interfacial layers, whereas axial heat transfer benefits from conduction along the current collectors. Experimental measurements have consistently reported much lower effective conductivity in the radial or through-plane direction than in the axial or in-plane direction [13, 14]. Bottom-up and inverse thermal-characterization studies have also shown that effective conductivity depends on layer composition, porosity, electrolyte saturation, geometry, and the way individual layers are combined [15, 16]. A meta-analysis of published battery thermal-property measurements found substantial scatter in through-plane conductivity and identified thermal contact resistance and battery-state dependencies as areas with limited experimental data [17]. The interface between the jelly roll and the case is an additional resistance: direct measurements of separator-to-case conductance showed large sample-to-sample variation [18]. In a cooled cell, a further resistance is introduced between the outer can and the cooling hardware. Its effective value depends on the interface material, bond-line thickness, contact quality, assembly pressure, and local geometry. Consequently, a temperature field obtained with one nominal radial conductivity and one nominal interface condition does not by itself establish how the cell will respond when either thermal resistance changes.

Direct measurement of the internal cell temperature is difficult during normal operation, even though the hottest region may occur beneath the can surface. In situ measurements with embedded thermocouples have demonstrated measurable radial temperature gradients in cylindrical cells and have shown that stronger cooling can lower the surface temperature while increasing the internal gradient [19]. This limitation has motivated a substantial body of work on virtual thermal sensing. Lin et al. developed a two-state thermal observer to estimate core temperature from surface measurements, while Richardson et al. combined surface temperature and impedance to estimate a non-uniform internal temperature distribution [20, 21]. Kim et al. showed explicitly that internal-temperature estimation depends on the cooling condition even when surface temperature is measured, and Richardson and Howey later demonstrated sensorless estimation using impedance and Kalman filtering [22, 23]. More recently, distributed three-dimensional electro-thermal models have been used to estimate internal temperature

from surface measurements with improved accuracy under aggressive loads [24]. A recent review of battery thermal-state monitoring reaches the same general conclusion: sparse external measurements do not fully describe the internal thermal state, and reliable estimation requires either additional physical information or a model that can reconstruct the spatial temperature field [25].

Machine-learning surrogates have recently been used to reduce the computational cost of battery thermal prediction by learning temperature responses from numerical or experimental datasets. A recent review of machine-learning-assisted battery thermal management identified temperature prediction and thermal-state diagnosis as major application areas [26]. Shen et al. combined a validated thermal model with convolutional neural networks to construct a digital-twin framework for rapid prediction of the temperature field in a large battery system [27]. Physics-informed neural networks have also been applied to large-format cells to improve temperature prediction with smaller datasets [28], while a recent universal-differential-equation approach demonstrated accurate heat-generation and temperature prediction with reduced experimental requirements [29]. However, in the studies reviewed here, model generalization is evaluated mainly across operating conditions such as current profiles, ambient conditions, or time-dependent loads; the thermal properties and contact resistances defining the cell's internal heat-conduction operator are generally prescribed during model construction.

Despite these developments, thermal-property uncertainty has received comparatively little attention in data-driven temperature-field reconstruction for 4680 cells. The 4680 thermal-management literature has established the importance of cell architecture, cooling topology, and thermal gradients, but most analyses are performed with a fixed or calibrated set of thermal properties [5, 7–12]. Conversely, internal-temperature estimation and recent machine-learning studies have made substantial progress in reconstructing hidden thermal states, but they generally address a particular cell parameterization and focus on changes in electrical or environmental operating conditions [20–29]. Accordingly, this study examines whether the can-surface temperature field can be reconstructed when radial jelly-roll conductivity and cell-to-cooler interface resistance are varied simultaneously. The relative influence of the spatial coordinates and thermal parameters is also evaluated.

A CFD-informed machine-learning framework was developed for a side-cooled 4680 cell. The thermal model follows the experimentally validated configuration reported by Allgäuer et al. [8]. A structured set of 75 steady CFD cases was generated by varying the jelly-roll radial thermal conductivity and an equivalent interface-layer thickness used as a controlled proxy for cell-to-cooler thermal resistance. Temperatures were sampled at 25 fixed can-surface locations in each CFD case, and the spatial coordinates together with the two thermal parameters were used as machine-learning inputs. Model development used point-wise data partitioning, five-fold cross-validation, z-score normalization, and Bayesian hyperparameter optimization. Model performance is evaluated using parity statistics and a Taylor diagram, followed by feature-importance, bootstrap, and error-distribution analyses. The trained surrogate is then used to reconstruct the can-surface temperature field at an interpolated parameter combination.

2. Methods

2.1. Numerical geometry and thermal model

A three-dimensional steady thermal model of a side-cooled Tesla 4680 Gen2 cylindrical cell was developed in ANSYS Fluent 2024 R2. The geometry follows the experimentally validated configuration of Allgäuer et al. [8]. The cell diameter and overall height are 46 and 80 mm, respectively, giving an outer radius of 23 mm. The aluminum side cooler covers a 60° circumferential sector and a 70 mm axial contact height, extending from z = -35 to + 35 mm about the cell mid-plane. The cooler thickness is 1 mm and the nickel-plated steel can is represented by a 0.35 mm wall. Geometry, cooler position, mesh topology, and all fixed material assignments were retained for the complete parametric campaign.

The computational domain contains only solid regions; no air or coolant domain was included. The model therefore solves steady three-dimensional heat conduction, with no fluid-flow or turbulence equations.

Table 1
Fixed geometry, materials, and thermal boundary conditions.

Region / parameter	Density (kg m^{-3})	c_p (J kg^{-1} K^{-1})	Conductivity / value	Basis
Cell diameter	—	—	46 mm	[8]
Cell height	—	—	80 mm	[8]
Jelly roll	2043	1371	$k_\theta = k_z = 23.1 W m^{-1} K^{-1}$; $k_r varied$	[8]
Electrolyte / empty core	1249	1642	$k = 0.2 W m^{-1} K^{-1}$	[8]
Housing (Ni-plated steel)	8030	600	$k = 60 W m^{-1} K^{-1}$	[8]
Negative terminal (Ni-plated steel)	8030	600	$k = 60 W m^{-1} K^{-1}$	[8]
Positive terminal (Aluminum)	2719	871	$k = 202 W m^{-1} K^{-1}$	[8]
Side cooler (Aluminum)	2719	871	$k = 202 W m^{-1} K^{-1}$; thickness = 1 mm	[8]
Interface layer	—	—	$k_{int} = 6.0 W m^{-1} K^{-1}$; tint varied	Present study
Cooler boundary	—	—	T = 25°C	[8]
Uncooled external surfaces	—	—	Adiabatic	Validated representation
Heat input	—	—	Q = 6.0 W in every case	Present study

The jelly roll was represented as an equivalent orthotropic solid because radial heat must cross the repeated electrode, separator, electrolyte, and interfacial layers, whereas heat spreads more readily in the axial and circumferential directions. The directional treatment is consistent with measured thermal anisotropy in cylindrical cells and with detailed conductivity studies [13, 15].

2.2. Governing equations and thermal boundary conditions

The transient solid-energy equation is

$$\rho\ c_p\ \partial T/\partial t\ =\ \nabla\ \cdot (\overline{\overline{k}}\ \nabla\ T)\ +\ q'''\quad (1)$$

where ρ is density, c_p is specific heat capacity, $\overline{\overline{k}}$ is the thermal-conductivity tensor, T is temperature, and q''' is the volumetric heat-generation rate. At steady state, the storage term vanishes:

$$\nabla\ \cdot (\overline{\overline{k}}\ \nabla\ T)\ +\ q'''\ =\ 0\quad (2)$$

For the orthotropic jelly roll, the thermal-conductivity tensor was defined in the local cylindrical coordinate system as

$$\overline{\overline{k}} =\ diag(k_r,\ k_\theta\ ,\ k_z)\quad (3)$$

The axial and circumferential conductivities were fixed at $k_z\ =\ k_\theta\ =\ 23.1\ W\ m^{-1}\ K^{-1}$, while k_r was varied as one of the study parameters. All other solid regions retained the validated isotropic properties listed in Table 1.

A constant total heat input of 6.0 W was applied uniformly to the positive-solid heat-source zone retained from the validated reduced model. The corresponding volumetric source is

$$q'''\ =\ \frac{Q}{V_{src}}\quad (4)$$

where Q = 6.0 W and V_{src} is the source-zone volume. The thermal load was fixed in all 75 simulations so that the effects of radial conductivity and cooler-interface resistance could be isolated.

The can-to-cooler contact was represented by an equivalent thin-wall thermal resistance. The interface conductivity was fixed at 6.0 W m⁻¹ K⁻¹ and the equivalent thickness t_{int} was varied. The area-specific resistance is

$$R''_{int}\ =\ \frac{t_{int}}{k_{t_{int}}}\quad (5)$$

The associated local temperature drop is related to the normal heat flux by

$$q''\ =\ \frac{(T_{can,int}\ -\ T_{cooler,int})}{R''_{int}}\quad (6)$$

The additional resistance was assigned once across the coupled wall pair to avoid double counting. The cooler boundary was maintained at 25°C, and all external surfaces outside the side-cooling contact were adiabatic. The investigated interface range was treated as a numerical sensitivity envelope rather than as a measured manufacturing tolerance. Battery-interface measurements show that interfacial thermal conductance can vary substantially with contact condition [18].

2.3. Mesh, validation, and numerical convergence

The mesh retained the same topology and local-refinement strategy used for the validated baseline model. Finer resolution was applied near the terminal region and the side-cooler contact, where the largest temperature gradients were expected.

The baseline model was validated against the three side-cooling temperatures reported by Allgäuer et al. [8]. The published values at Sensors 0, 2, and 3 are 25.0, 35.6, and 39.8°C, respectively, while the present predictions are 25.030, 35.483, and 39.604°C. The maximum absolute difference is 0.196°C and the largest relative deviation is 0.493%.

Grid convergence was assessed using meshes containing 1,038,071, 2,594,777, and 3,948,213 elements. At the three validation locations, the difference between the two finest meshes was below 0.01%; the maximum Grid 2 to Grid 3 relative change was 0.0081% at Sensor 3. The 2,594,777-element mesh was retained for the full 75-case campaign.

All simulations were advanced to a steady converged state using the same numerical procedure. The energy residual was reduced to 10^{-8}, and monitored temperatures were required to become stationary before post-processing.

2.4. Thermal-property design and surface-temperature database

Two parameters were varied independently while geometry, mesh, heat input, cooler temperature, and all other material properties were kept fixed. The radial jelly-roll conductivity k_r was assigned 15 levels: 0.90, 0.95, 1.00, 1.05, 1.10, 1.20, 1.30, 1.40, 1.50, 1.60, 1.70, 1.80, 1.90, 1.95, and 2.00 W m^{-1} K^{-1}. The equivalent interface thickness t_{int} was assigned five levels: 0.40, 0.45, 0.50, 0.55, and 0.60 mm. With k_{int} fixed at 6.0 W m^{-1} K^{-1}, these values correspond to area-specific interface resistances from 6.667×10^{-5} to 1.000×10^{-4} m² K W^{-1}. The full factorial combination produced 75 independent steady CFD conditions; Q = 6.0 W and the cooler temperature of 25°C were fixed throughout.

For each CFD condition, temperature was extracted at 25 fixed locations on the accessible outer-can surface. Five axial levels, $z = -32,\ -16,\ 0,\ +16,\ and\ +32\ mm$, were combined with five circumferential positions, $\theta = 60^\circ,\ 120^\circ,\ 180^\circ,\ 240^\circ,\ and\ 300^\circ$, forming a 5×5 grid. The cooler centerline defines $\theta = 0^\circ$. The physical radius is 23 mm; the Fluent point probes were placed 0.010 mm inside the steel wall to avoid point-location failures at the exact boundary.

Each pointwise record contained five predictors:

$$X = [x,\ y,\ z,\ k_r,\ t_{int}] \quad (7)$$

with local CFD temperature as the response. The full database therefore contained 75 × 25 = 1,875 spatial observations.

2.5. Machine-learning data preparation and validation strategy

The machine-learning analysis was performed in MATLAB R2024b using the Statistics and Machine Learning Toolbox and the Deep Learning Toolbox. The dataset was partitioned at the level of individual spatial samples rather than by complete CFD case. Five-fold cross-validation was used during model development, with a random seed of 42 for data partitioning.

All predictors were standardized using z-score normalization:

$$x^* = (x - \mu) / \sigma \quad (8)$$

where μ and σ are the mean and standard deviation used for scaling. Hyperparameters were selected by Bayesian optimization. The coefficient of determination and RMSE values shown in the parity plots were calculated only from the held-out test subset, and the Taylor diagram used predictions from the same test subset.

The point-wise split allowed spatial samples from the same CFD condition to occur in different partitions. Accordingly, the reported test metrics describe interpolation of held-out spatial samples within the simulated design space and may be more optimistic than results obtained using case-wise grouped validation [30].

2.6. Regression models and optimized settings

Three regression approaches were used: a convolutional neural network-long short-term memory model (CNN-LSTM), support vector regression (SVM), and a multilayer perceptron (MLP). SVM served as a non-neural kernel-based comparator, while the MLP provided a fully connected nonlinear baseline. Hyperparameters were selected using Bayesian optimization on the development data. The support-vector formulation follows the standard regression framework described by Smola and Schölkopf [32].

For CNN-LSTM, the 25 surface locations were arranged in their numerical sensor order before sequence processing. The sequence begins with VS01-VS05 at z = -32 mm, followed by the rings at $z = -16,\ 0,\ +16$, and $+32$ mm. Within each axial ring, the circumferential order is $\theta = 60^\circ,\ 120^\circ,\ 180^\circ,\ 240^\circ,\ and\ 300^\circ$. The LSTM component follows the standard long short-term memory formulation [31].

The final CNN-LSTM configuration used 52 one-dimensional convolution filters, 16 LSTM hidden units, a dropout rate of 0.112, a mini-batch size of 89, and an initial learning rate of 7.726323×10^{-4}. Training used the Adam optimizer for 300 epochs; Bayesian-objective evaluations used 100 epochs, early stopping was not applied, and the random seed was 42. The regression loss was the half-mean-squared-error implemented by MATLAB regression Layer. The MLP used two hidden layers containing 284 and 49 neurons with tanh activation.

2.7. Prediction metrics and comparative diagnostics

Prediction performance was quantified on the held-out point-level test subset using the coefficient of determination (R^2) and root-mean-square error (RMSE):

$$R^2 = 1 - \Sigma (T - \hat{T})^2 / \Sigma (T - \bar{T})^2 \quad (9)$$

$$RMSE = \sqrt{[(1/N) \Sigma (T - \hat{T})^2]} \quad (10)$$

Parity plots were used to compare CFD and predicted temperatures. A Taylor diagram was generated from the same held-out test predictions to summarize correlation coefficient, standard deviation, and centered error relative to the CFD reference [33].

2.8. Feature importance, bootstrap uncertainty, and error distribution

Feature importance was evaluated for the CNN-LSTM model. The analysis reports the increase in RMSE associated with perturbing each predictor; larger ΔRMSE indicates a stronger contribution to predictive performance. The resulting ranking was interpreted with care because x and y jointly encode circumferential position on a fixed-radius cylinder.

Bootstrap uncertainty was also evaluated for CNN-LSTM using 3,000 bootstrap repetitions. The resulting empirical RMSE distribution was used to assess the stability of the reported prediction error, following the general bootstrap framework [34].

Finally, the distribution of absolute prediction error, $|T_{CFD} - T_{pred}|$, was visualized for CNN-LSTM, SVM, and MLP using a beeswarm representation. This diagnostic complements the scalar RMSE value by showing the dense low-error population together with less frequent larger deviations.

2.9. Parametric response maps and surface reconstruction

The trained surrogate was used as a post-processing model to examine the coupled response to k_r and t_{int} at three representative axial levels, $z = -32,\ 0,\ and\ +32\ mm$; the middle plane is therefore z = 0 mm. The surface-coordinate convention defined in Section 2.4 was retained while $k_r$and t_{int}were varied across the prescribed ranges.

A separate three-dimensional surface visualization was generated for $k_r = 1.35\ W\ m^{-2}\ K^{-1}$ and $t_{int} = 0.52\ mm$. This parameter pair lies inside the investigated numerical envelope but is not one of the 75 discrete CFD design points. The trained surrogate predictions were mapped onto the cylindrical can surface to visualize the interpolated surface-temperature field. Because no additional CFD case was run at this exact pair, the reconstruction is presented as surrogate interpolation rather than as an independent CFD validation or a volumetric internal-temperature solution.

2.10. Scope and methodological limitations

The numerical framework is restricted to steady-state thermal behavior with a fixed 6.0 W heat input and a prescribed 25°C side-cooling boundary. Temperature-dependent electrochemical heat generation, transient storage, external convection and radiation, aging-related property changes, and thermal-runaway chemistry are outside the present model.

The models were trained from CFD-derived spatial samples and the data split was performed at the point level. Consequently, the reported held-out performance demonstrates interpolation of unsampled spatial records inside the simulated thermal-property domain; it does not constitute an operator-level test on completely unseen CFD cases. The 3D surface map at $k_r = 1.35\,W\,m^{-1}K^{-1}$ and $t_{int} = 0.52\,mm$ is likewise an interpolated surrogate visualization rather than a direct numerical validation case.

3. Results and Discussion

3.1. Prediction performance of the machine-learning models

Figure 5 compares the test-set predictions from CNN-LSTM, SVM, and MLP with the corresponding CFD temperatures. CNN-LSTM and SVM follow the 1:1 line closely over most of the approximately 28–36°C temperature range. CNN-LSTM achieved R^2 = 0.981 with an RMSE of 0.238°C, while SVM gave R^2 = 0.980 and an RMSE of 0.245°C. The difference between these two models is therefore small: their R^2 values differ by only 0.001 and their RMSE values by 0.007°C. In contrast, the MLP produced visibly larger scatter, particularly in the middle of the temperature range, with R^2 = 0.817 and an RMSE of 0.685°C.

The Taylor diagram in Fig. 5d confirms the similarity between CNN-LSTM and SVR. Both markers lie close to the CFD reference, indicating similar correlation and variance relative to the test data. The MLP is farther from the reference, consistent with the broader scatter in its parity plot. CNN-LSTM and SVR therefore provide nearly identical global accuracy for the present dataset, whereas the MLP shows substantially greater prediction scatter.

The low global RMSE values of CNN-LSTM and SVM should not be interpreted as uniform sub-0.25°C accuracy at every spatial point. Both parity plots contain a small number of localized departures from the 1:1 line. Moreover, because the test data were produced using the point-wise partition described in Section 2.5, these statistics quantify interpolation of held-out spatial samples within the simulated parameter domain rather than independent generalization to completely unseen CFD operators.

3.2. Feature importance, uncertainty, and error structure

Figure 6a shows that axial position $z$has the largest influence on prediction accuracy, increasing RMSE by approximately 1.8°C when perturbed. The $x$coordinate is second at about 1.4°C, followed by radial thermal conductivity at roughly 0.5°C. The contributions associated with y position and interface resistance are much smaller, both remaining below approximately 0.1°C in this analysis. The dominant

role of $z$reflects the axial non-uniformity produced by the finite-height cooling contact. The importance of x likewise reflects circumferential variation around the side-cooled surface. The influence of radial conductivity agrees with previous experimental and modeling studies showing that radial heat transfer in cylindrical jelly rolls is more resistive than axial and circumferential heat transfer [13, 15].

The comparatively small interface-resistance importance should be interpreted only within the narrow 0.40–0.60 mm equivalent-thickness range examined here; it does not imply that cell-to-cooler resistance is generally unimportant outside this range.

The 3,000 bootstrap samples in Fig. 6b produced an RMSE distribution centered near 0.26°C, with most values between approximately 0.22 and 0.29°C. The distribution is slightly shifted above the single test-set RMSE of 0.238°C, reflecting changes in sample composition across the resamples.

Figure 6c shows the point-wise absolute-error distribution for the three models. CNN-LSTM and SVM both contain dense concentrations of very small absolute errors, but each also exhibits a limited tail of larger deviations reaching approximately 2.5°C. The MLP distribution is noticeably broader and includes errors approaching 5°C. The larger MLP RMSE is therefore associated with both broader overall scatter and a greater number of large local errors.

3.3. Three-dimensional surrogate surface-temperature reconstruction

Figure 7 presents the surrogate surface-temperature field for $k_r = 1.35\ W\ m^{-1}\ K^{-1}$ and $t_{int} = 0.52\ mm$. This parameter pair lies within the numerical envelope used for model development but does not coincide with one of the 75 discrete CFD design points. The predicted can-surface temperature varies from approximately 28.5°C in the coolest region to slightly above 35°C in the warmest region. A clear axial gradient is visible, with higher temperatures concentrated toward the upper part of the cell, while a substantial circumferential variation is also retained.

The reconstructed field varies most strongly in the axial and circumferential directions, in agreement with the feature ranking in Fig. 6a. The reconstruction illustrates how the trained surrogate interpolates the surface field between the discrete parameter combinations used in the CFD database. It should, however, be interpreted as an interpolation of the external can-surface temperature field. No additional CFD simulation was performed at the exact $k_r = 1.35\ W\ m^{-1}\ K^{-1}$ and $t_{int} = 0.52\ mm$ combination, so Fig. 7 is not an independent validation case and does not represent the internal volumetric temperature field.

3.4. Implications of the combined CFD-ML analysis

For the present side-cooled configuration, spatial position has a larger influence on predicted surface temperature than either of the two varied thermal parameters. The ML models therefore learn both the spatial temperature pattern and its modification by k_r and t_{int}, rather than a simple two-parameter

temperature relation. CNN-LSTM and SVM capture that mapping with similar global accuracy, whereas the present MLP configuration does not reproduce the localized thermal structure as consistently.

The CFD database represents steady conditions at a fixed 6 W heat input and a 25°C side-cooling boundary, and the ML test set was created by point-wise partitioning. The results therefore support rapid interpolation of the simulated surface field within this domain, but they should not be extrapolated to different heat loads, cooling arrangements, transient operation, or completely unseen thermal operators without additional validation.

4. Conclusions

This study combined a validated steady CFD model with three regression methods to predict the can-surface temperature of a side-cooled 4680 cell under variations in radial conductivity and interface resistance. The underlying thermal model reproduced the three published validation temperatures within 0.196°C, and the two finest meshes changed the monitored temperatures by less than 0.01%. A total of 75 steady CFD conditions generated 1,875 spatial temperature records for machine-learning analysis.

Among the three models, CNN-LSTM and SVR gave nearly identical point-level test performance. CNN-LSTM achieved R^2 = 0.981 and RMSE = 0.238°C, while SVM achieved R^2 = 0.980 and RMSE = 0.245°C. The MLP was less accurate, with R^2 = 0.817 and RMSE = 0.685°C, and its error distribution contained substantially larger outliers. The Taylor diagram and absolute-error distributions also show the larger scatter associated with the MLP.

Feature perturbation showed that axial position was the strongest predictor of the surface temperature, followed by the x coordinate and radial conductivity. The effects associated with y position and the interface-resistance range investigated were comparatively small. The 3,000 bootstrap samples produced an RMSE distribution centered near 0.26°C. The surrogate was also used to reconstruct the can-surface field at $k_r = 1.35\ W\ m^{-1}\ K^{-1}$ and $t_{int} = 0.52\ mm$, producing a smooth axial and circumferential temperature pattern within the trained parameter envelope.

The present results should be interpreted as interpolation within a steady, fixed-load CFD database. Because individual spatial points rather than complete CFD cases were separated during machine-learning partitioning, the reported test metrics do not constitute independent validation on unseen thermal operators. Likewise, the three-dimensional surface reconstruction was not checked by an additional CFD run at the exact interpolated condition. Within the investigated steady-state domain, CNN-LSTM and SVM reproduced the CFD-derived surface-temperature field with RMSE values below 0.25°C. Further case-wise validation would be required before extending the models to unseen thermal operators or operating conditions.

Declarations

CRediT authorship contribution statement

Aydin Ulus: Conceptualization, Methodology, Investigation, Validation, Formal analysis, Data curation, Visualization, Writing – original draft.

Ihsan Uluocak: Methodology, Software, Formal analysis, Data curation, Visualization.

Wajih Nazim Kamal: Investigation, Data curation.

Young Jik Youn: Writing – review & editing.

Kyosung Choo: Supervision, Writing – review & editing.

Competing interests

The authors declare no competing interests.

Funding

This research received no external funding.

Author Contribution

Aydin Ulus: Conceptualization, Methodology, Investigation, Validation, Formal analysis, Data curation, Visualization, Writing – original draft.Ihsan Uluocak: Methodology, Software, Formal analysis, Data curation, Visualization.Wajih Nazim Kamal: Investigation, Data curation.Young Jik Youn: Writing – review & editing.Kyosung Choo: Supervision, Writing – review & editing.

Acknowledgements

This work was supported by the research fund of Hanbat National University in 2024.

Data Availability

The data supporting the findings of this study are available from the corresponding author upon reasonable request.

References

1. Bernardi, D., Pawlikowski, E. & Newman, J. A general energy balance for battery systems. *J. Electrochem. Soc.* **132**, 5–12. https://doi.org/10.1149/1.2113792 (1985).
2. Bandhauer, T. M., Garimella, S. & Fuller, T. F. A critical review of thermal issues in lithium-ion batteries. *J. Electrochem. Soc.* **158**, R1–R25. https://doi.org/10.1149/1.3515880 (2011).
3. Troxler, Y. et al. The effect of thermal gradients on the performance of lithium-ion batteries. *J. Power Sources*. **247**, 1018–1025. https://doi.org/10.1016/j.jpowsour.2013.06.084 (2014).
4. Waldmann, T. et al. Influence of cell design on temperatures and temperature gradients in lithium-ion cells: An in operando study. *J. Electrochem. Soc.* **162**, A921–A927. https://doi.org/10.1149/2.0561506jes (2015).
5. Tranter, T. G., Timms, R., Shearing, P. R. & Brett, D. J. L. Communication—Prediction of thermal issues for larger format 4680 cylindrical cells and their mitigation with enhanced current collection. *J. Electrochem. Soc.* **167**, 160544. https://doi.org/10.1149/1945-7111/abd44f (2020).
6. Ank, M. et al. Lithium-ion cells in automotive applications: Tesla 4680 cylindrical cell teardown and characterization. *J. Electrochem. Soc.* **170**, 120536. https://doi.org/10.1149/1945-7111/ad14d0 (2023).
7. Li, S., Marzook, M. W., Zhang, C., Offer, G. J. & Marinescu, M. How to enable large format 4680 cylindrical lithium-ion batteries. *Appl. Energy*. **349**, 121548. https://doi.org/10.1016/j.apenergy.2023.121548 (2023).
8. Allgäuer, C., Grenz, F., Abo Gamra, K. & Lienkamp, M. Thermal management of 4680 battery cells: Cell design and cooling concept. *J. Energy Storage*. **131**, 117318. https://doi.org/10.1016/j.est.2025.117318 (2025).
9. Allgäuer, C. et al. Thermal management of 4680 battery cells during fast charging: Mitigating degradation and revealing major reversible capacity recovery. *eTransportation* **28**, 100574. https://doi.org/10.1016/j.etran.2026.100574 (2026).
10. Paz, C., Vence, J., Bouzas-Jamardo, N. & Conde-Fontenla, M. Thermal management of 4680 cylindrical cells with cold plate strategies: Comparative performance of sided and terminal layouts. *J. Energy Storage*. **154**, 121001. https://doi.org/10.1016/j.est.2026.121001 (2026).
11. Li, C. et al. Two-phase immersion liquid cooling system for 4680 Li-ion battery thermal management. *J. Energy Storage*. **97**, 112952. https://doi.org/10.1016/j.est.2024.112952 (2024).
12. Yasrebi, S., Ashjaee, M. & Houshfar, E. Extreme fast charging performance of 4680 lithium-ion batteries: Thermo-electrochemical analysis of chemistry effects. *J. Energy Storage*. **132**, 117981. https://doi.org/10.1016/j.est.2025.117981 (2025).
13. Drake, S. J. et al. Measurement of anisotropic thermophysical properties of cylindrical Li-ion cells. *J. Power Sources*. **252**, 298–304. https://doi.org/10.1016/j.jpowsour.2013.11.107 (2014).
14. Maleki, H., Al Hallaj, S., Selman, J. R., Dinwiddie, R. B. & Wang, H. Thermal properties of lithium-ion battery and components. *J. Electrochem. Soc.* **146**, 947–954. https://doi.org/10.1149/1.1391704 (1999).

15. Werner, D., Loges, A., Becker, D. J. & Wetzel, T. Thermal conductivity of Li-ion batteries and their electrode configurations—A novel combination of modelling and experimental approach. *J. Power Sources*. **364**, 72–83. https://doi.org/10.1016/j.jpowsour.2017.07.105 (2017).
16. Al-Zareer, M., Michalak, A., Da Silva, C. & Amon, C. H. Predicting specific heat capacity and directional thermal conductivities of cylindrical lithium-ion batteries: A combined experimental and simulation framework. *Appl. Therm. Eng.* **182**, 116075. https://doi.org/10.1016/j.applthermaleng.2020.116075 (2021).
17. Steinhardt, M. et al. Meta-analysis of experimental results for heat capacity and thermal conductivity in lithium-ion batteries: A critical review. *J. Power Sources*. **522**, 230829. https://doi.org/10.1016/j.jpowsour.2021.230829 (2022).
18. Gaitonde, A., Nimmagadda, A. & Marconnet, A. Measurement of interfacial thermal conductance in lithium ion batteries. *J. Power Sources*. **343**, 431–436. https://doi.org/10.1016/j.jpowsour.2017.01.019 (2017).
19. Zhang, G. et al. In situ measurement of radial temperature distributions in cylindrical Li-ion cells. *J. Electrochem. Soc.* **161**, A1499–A1507. https://doi.org/10.1149/2.0051410jes (2014).
20. Lin, X. et al. Online parameterization of lumped thermal dynamics in cylindrical lithium ion batteries for core temperature estimation and health monitoring. *IEEE Trans. Control Syst. Technol.* **21**, 1745–1755. https://doi.org/10.1109/TCST.2012.2217143 (2013).
21. Richardson, R. R., Ireland, P. T. & Howey, D. A. Battery internal temperature estimation by combined impedance and surface temperature measurement. *J. Power Sources*. **265**, 254–261. https://doi.org/10.1016/j.jpowsour.2014.04.129 (2014).
22. Kim, Y., Mohan, S., Siegel, J. B., Stefanopoulou, A. G. & Ding, Y. The estimation of temperature distribution in cylindrical battery cells under unknown cooling conditions. *IEEE Trans. Control Syst. Technol.* **22**, 2277–2286. https://doi.org/10.1109/TCST.2014.2309492 (2014).
23. Richardson, R. R. & Howey, D. A. Sensorless battery internal temperature estimation using a Kalman filter with impedance measurement. *IEEE Trans. Sustain. Energy*. **6**, 1190–1199. https://doi.org/10.1109/TSTE.2015.2420375 (2015).
24. Li, S. et al. Internal temperature estimation for lithium-ion batteries through distributed equivalent circuit network model. *J. Power Sources*. **611**, 234701. https://doi.org/10.1016/j.jpowsour.2024.234701 (2024).
25. Zheng, Y. et al. Thermal state monitoring of lithium-ion batteries: Progress, challenges, and opportunities. *Prog. Energy Combust. Sci.* **100**, 101120. https://doi.org/10.1016/j.pecs.2023.101120 (2024).
26. Li, A. et al. Machine learning assisted advanced battery thermal management system: A state-of-the-art review. *J. Energy Storage*. **60**, 106688. https://doi.org/10.1016/j.est.2023.106688 (2023).
27. Shen, K. et al. A deep learning-based digital twin model for the temperature field of large-scale battery systems. *J. Energy Storage*. **113**, 115676. https://doi.org/10.1016/j.est.2025.115676 (2025).

28. Shen, K. et al. Physics-informed machine learning estimation of the temperature of large-format lithium-ion batteries under various operating conditions. *Appl. Therm. Eng.* **269**, 126200. https://doi.org/10.1016/j.applthermaleng.2025.126200 (2025).
29. Kalathingal, A., Ayyangatu Kuzhiyil, J., Grandjean, T. & Dinh, Q. T. Faraji Niri, M. Physics-informed machine learning for battery heat generation estimation and temperature prediction with minimal experimentation. *Energy AI*. **25**, 100808. https://doi.org/10.1016/j.egyai.2026.100808 (2026).
30. Roberts, D. R. et al. Cross-validation strategies for data with temporal, spatial, hierarchical, or phylogenetic structure. *Ecography* **40**, 913–929. https://doi.org/10.1111/ecog.02881 (2017).
31. Hochreiter, S. & Schmidhuber, J. Long short-term memory. *Neural Comput.* **9**, 1735–1780. https://doi.org/10.1162/neco.1997.9.8.1735 (1997).
32. Smola, A. J. & Schölkopf, B. A tutorial on support vector regression. *Stat. Comput.* **14**, 199–222. https://doi.org/10.1023/B:STCO.0000035301.49549.88 (2004).
33. Taylor, K. E. Summarizing multiple aspects of model performance in a single diagram. *J. Geophys. Research: Atmos.* **106**, 7183–7192. https://doi.org/10.1029/2000JD900719 (2001).
34. Efron, B. Bootstrap methods: Another look at the jackknife. *Annals Stat.* **7**, 1–26. https://doi.org/10.1214/aos/1176344552 (1979).

Figures

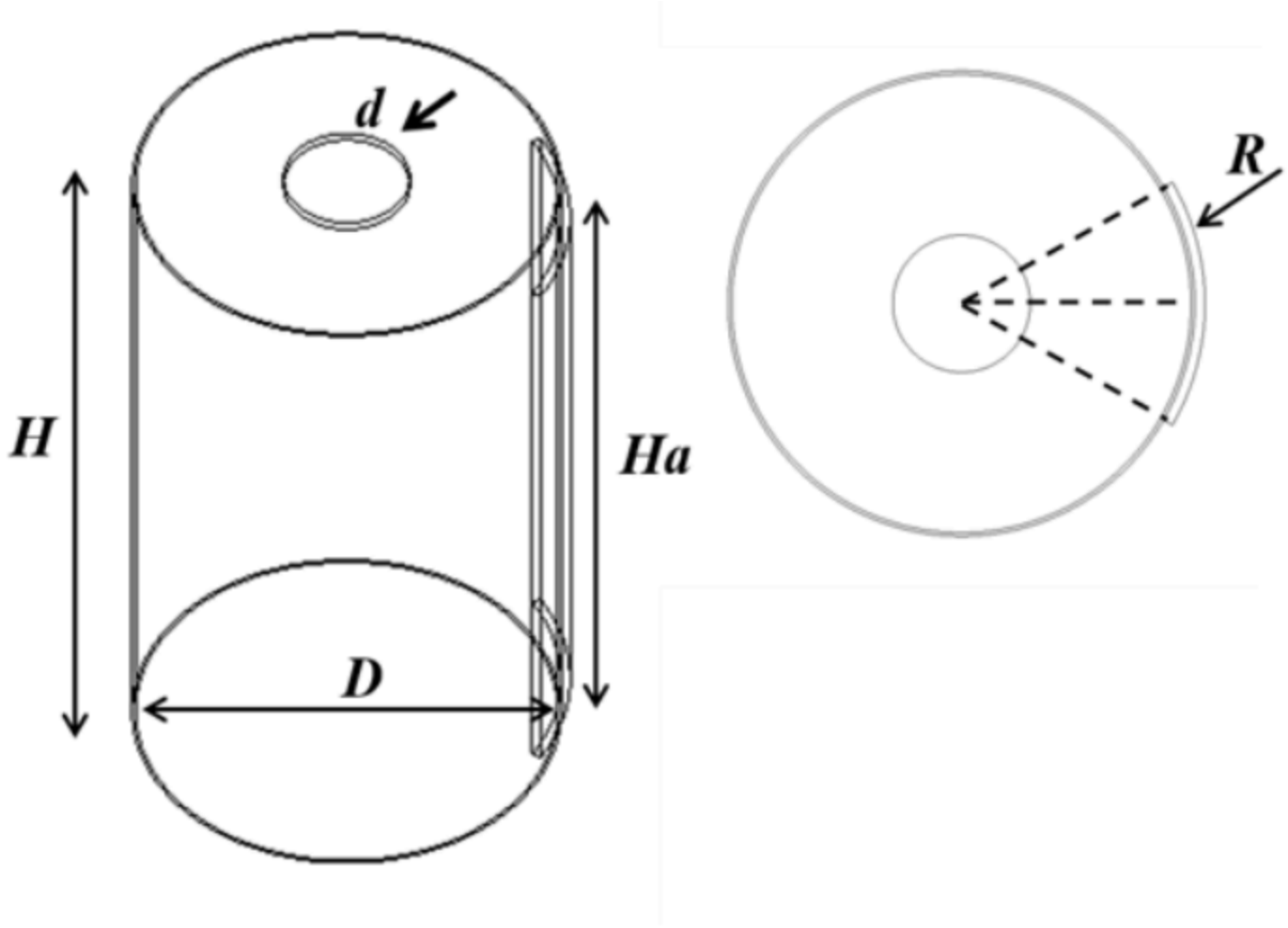


Figure 1

Geometry of the 4680 Gen2 cell and side-cooling contact. The geometric basis follows the validated configuration of Allgäuer et al. [8].

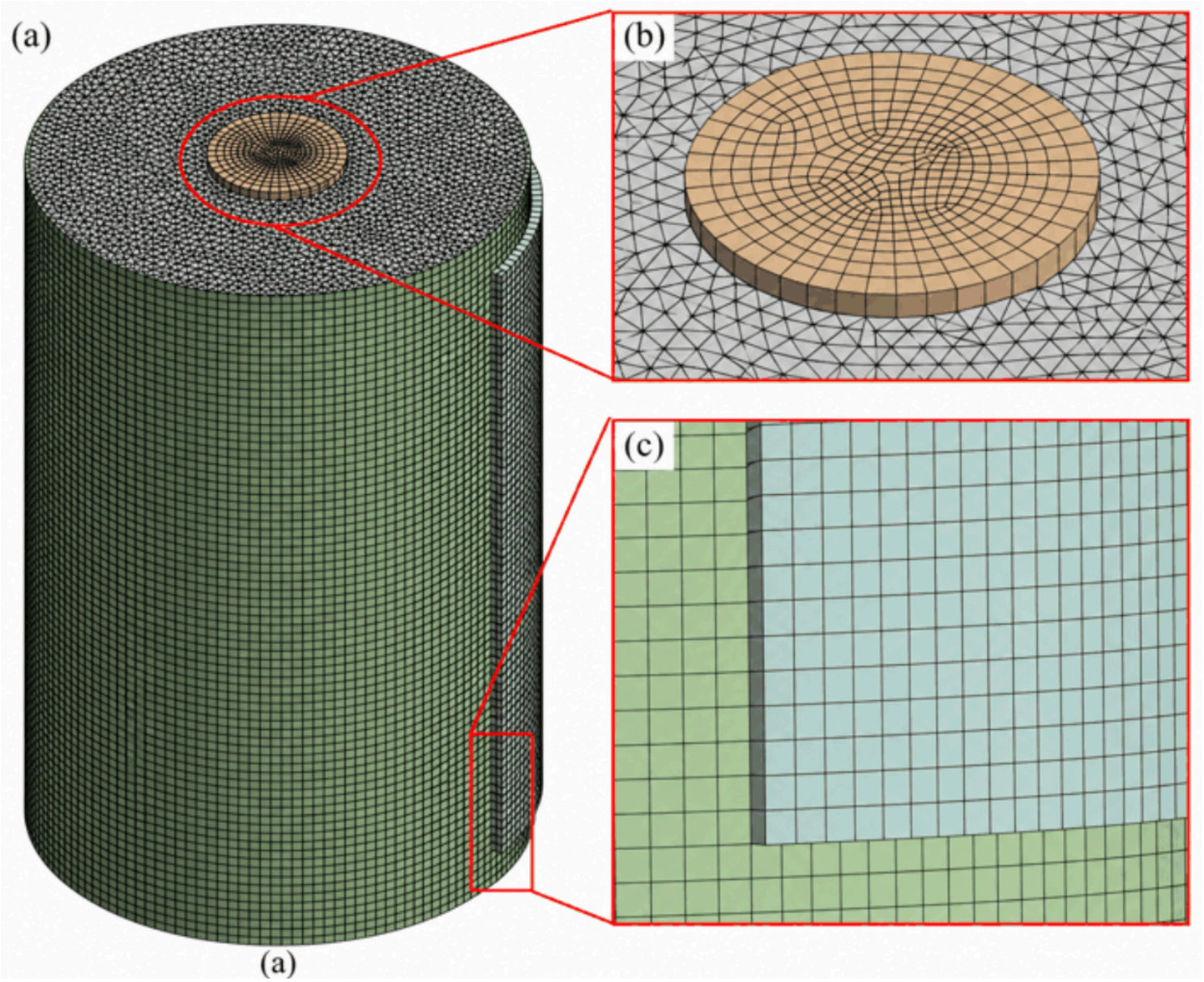


Figure 2

Computational mesh of the three-dimensional 4680 thermal model, including local refinement near the terminal and cooler-contact regions.

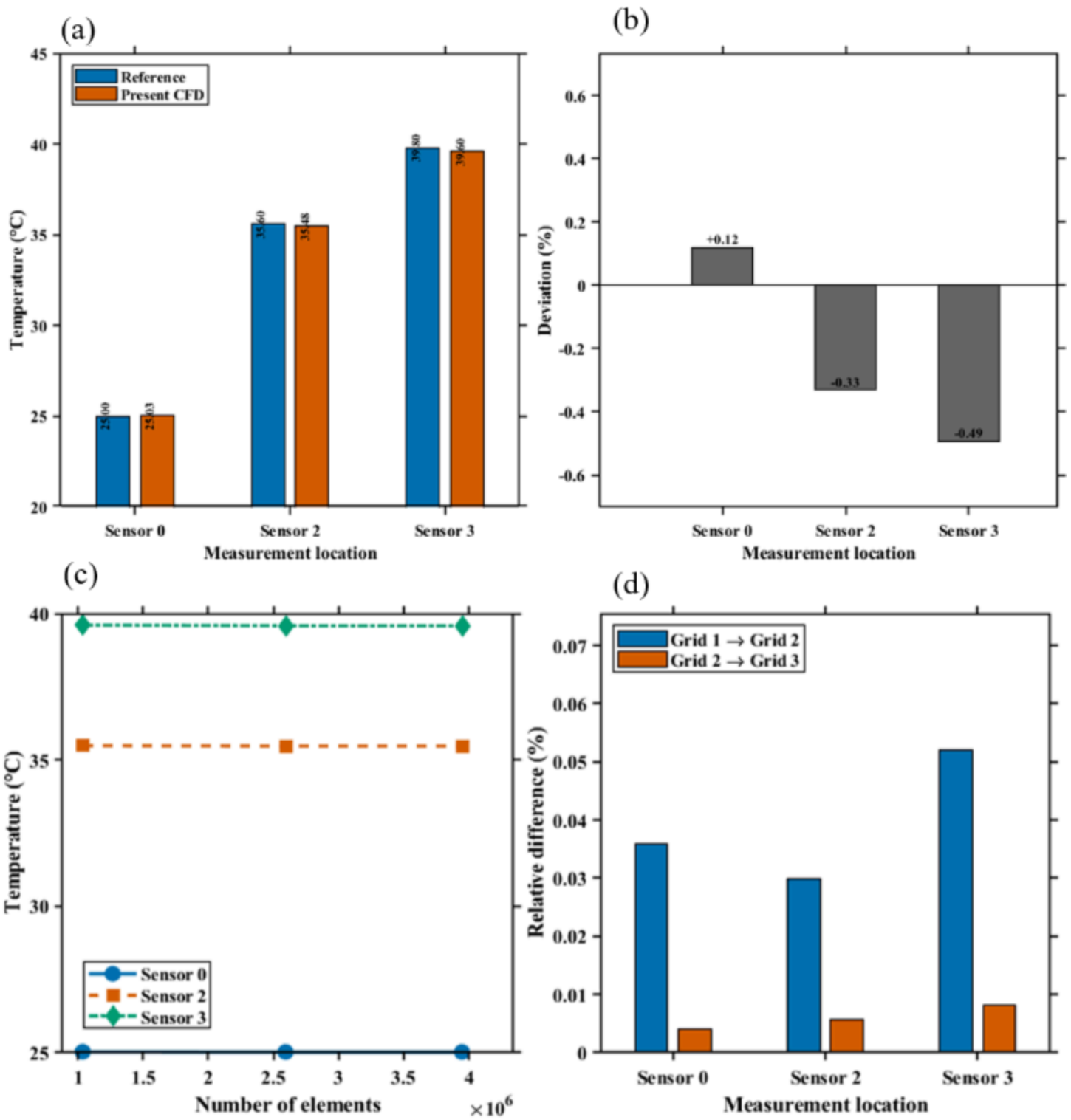


Figure 3

Validation against the published side-cooling temperatures and grid-convergence behavior at the monitored locations.

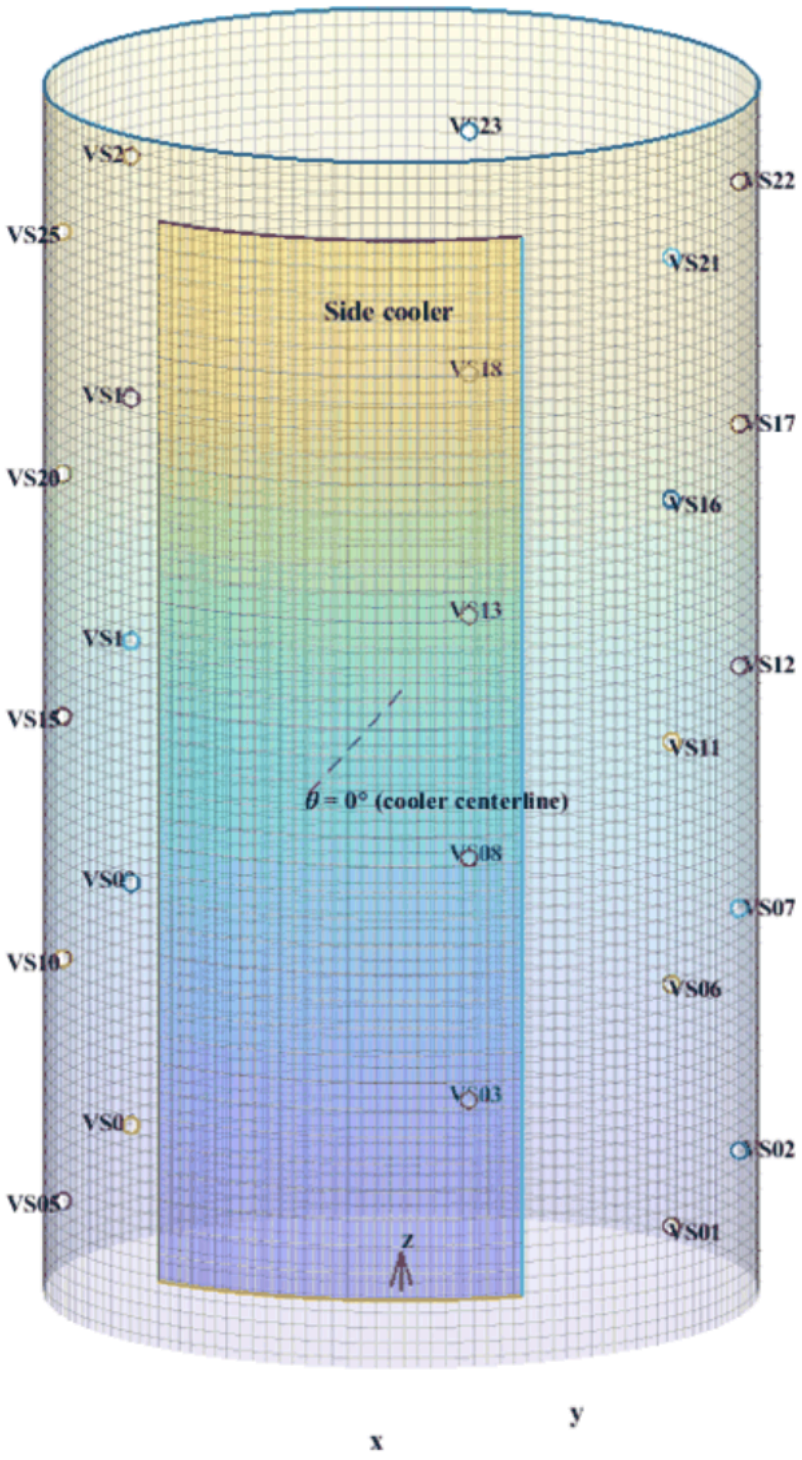


Figure 4

Fixed 25-point surface-temperature sampling layout. Sensor numbering proceeds ring by ring from z = -32 mm to z = +32 mm.

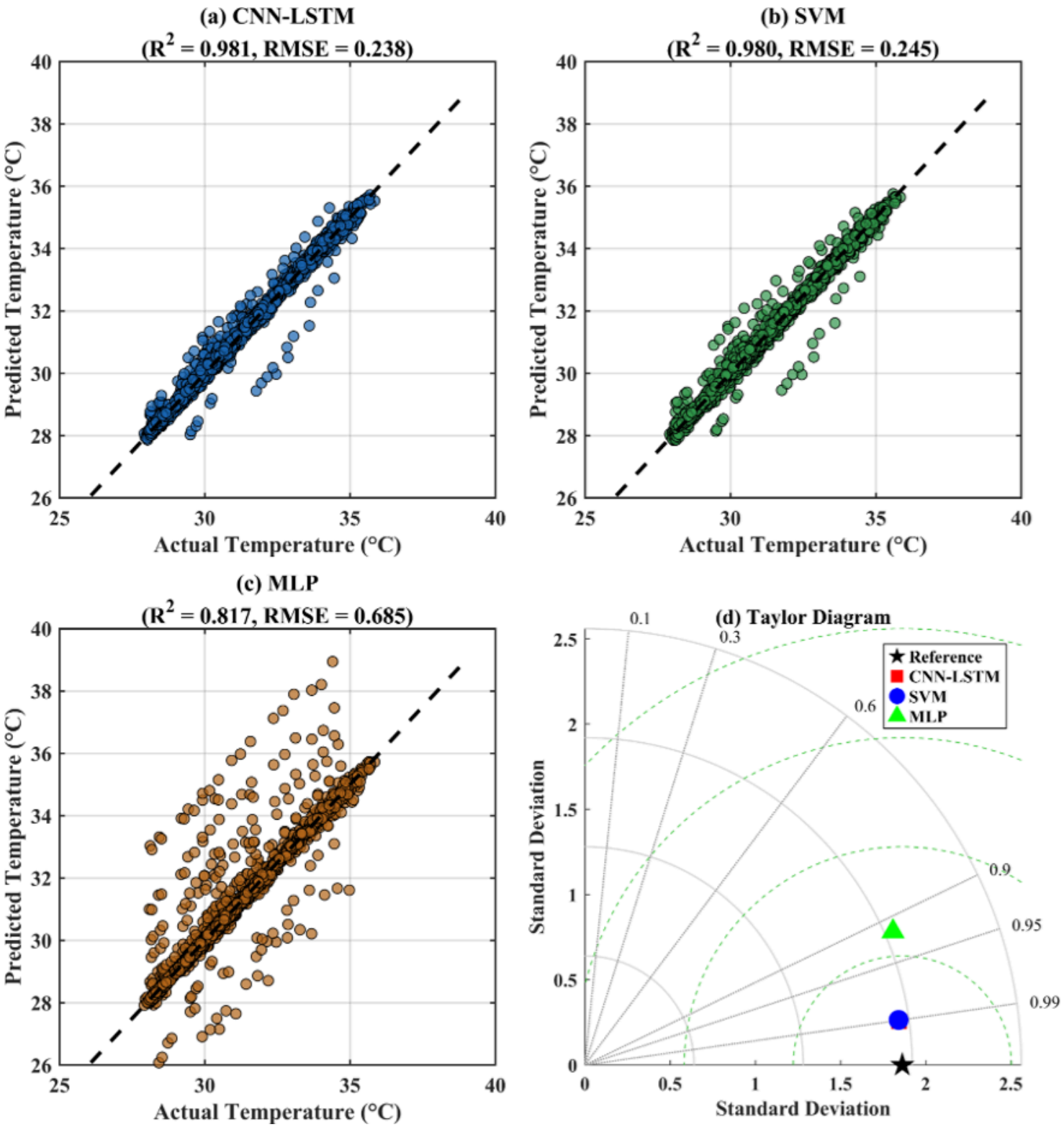


Figure 5

Test-set prediction performance for (a) CNN-LSTM, (b) SVM, and (c) MLP, together with (d) the Taylor diagram. The dashed line in the parity plots denotes ideal agreement between CFD and machine-learning predictions.

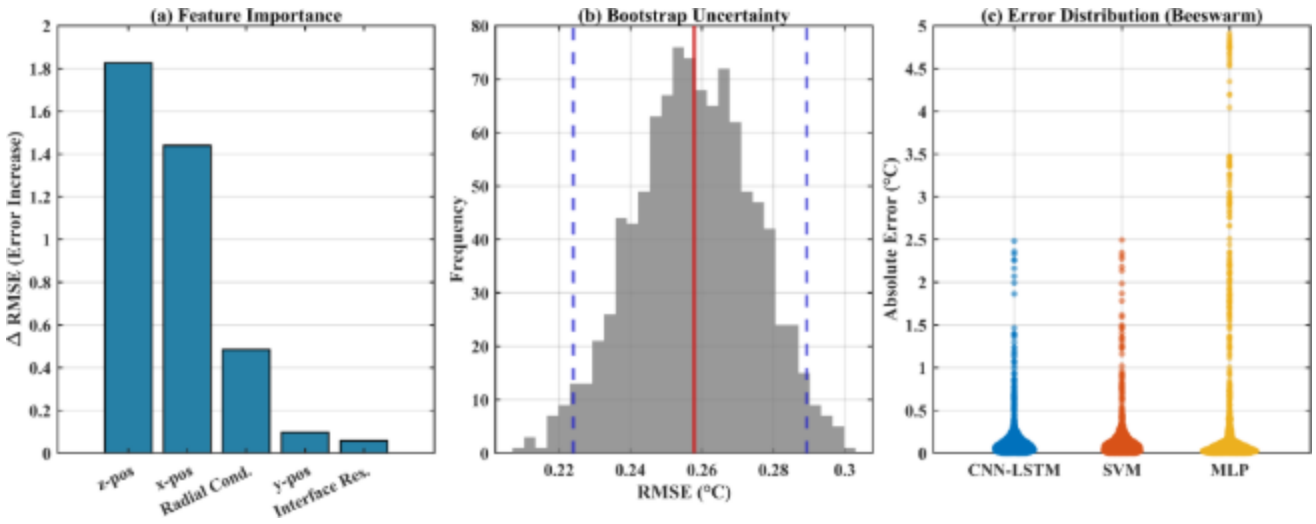


Figure 6

Interpretation and uncertainty analysis: (a) CNN-LSTM feature importance expressed as the increase in RMSE, (b) bootstrap distribution of CNN-LSTM RMSE from 3,000 resamples, and (c) absolute-error distributions for CNN-LSTM, SVM, and MLP.

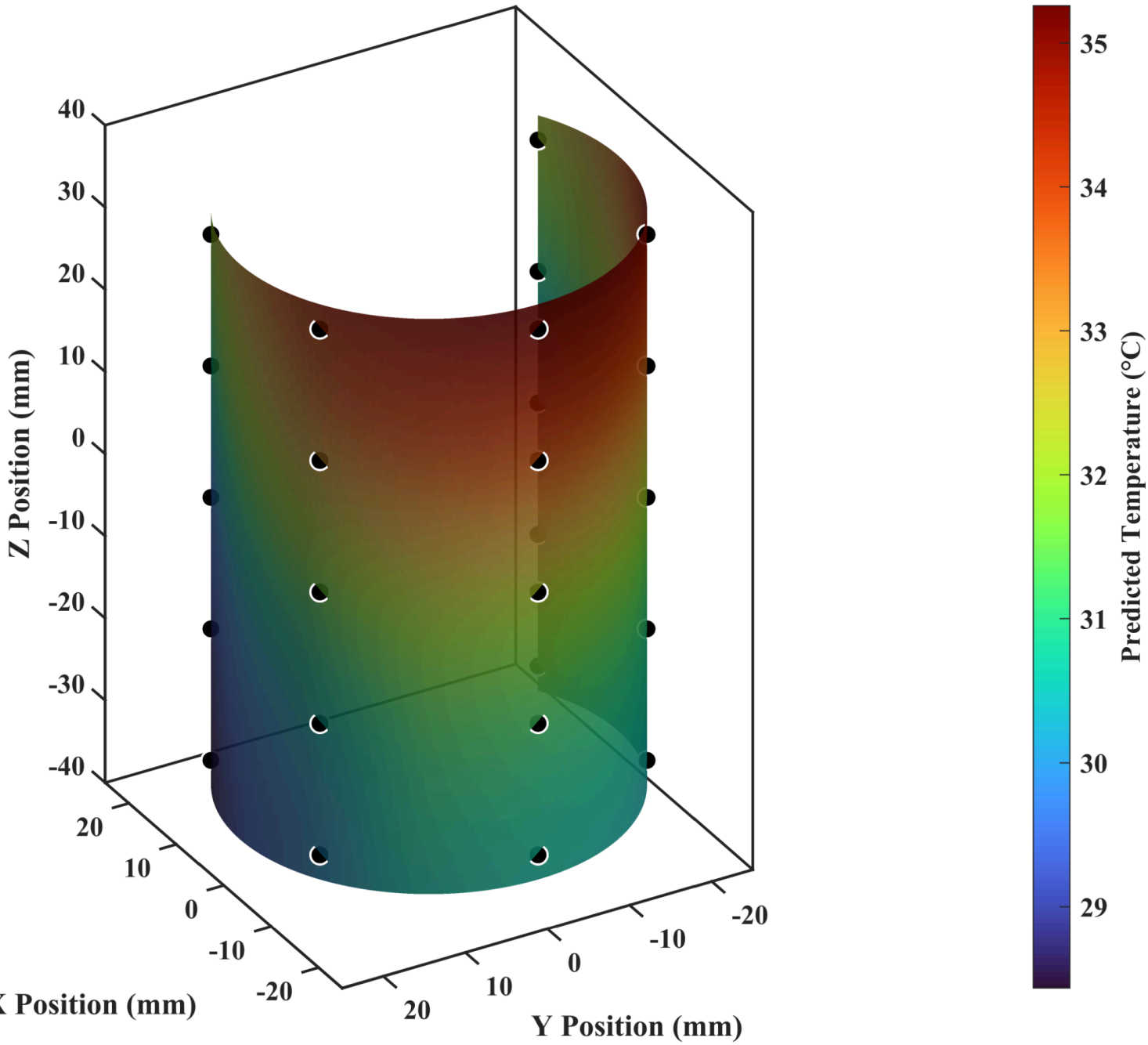


Figure 7

Three-dimensional surrogate reconstruction of the external can-surface temperature field for kr = 1.35 W m^{-1} K^{-1} and t_int = 0.52 mm. The parameter pair lies inside the investigated design space but was not one of the 75 discrete CFD conditions.